Synthesis of Superlattices of Intercalated Transition Metal Dichalcogenides

T. A. Hughes,[†] S. D. Kevan,[†] D. E. Cox,[‡] and D. C. Johnson*[,§]

Contribution from the Departments of Physics and Chemistry, University of Oregon, Eugene, Oregon 97403, and Brookhaven National Laboratory, Upton, New York 11973-5000

Received November 29, 1999. Revised Manuscript Received July 17, 2000

Abstract: Thin films of oriented Fe and Cr intercalated $(NbSe_2)_x(TiSe_2)_y$ superlattices have been synthesized by controlled annealing of elementally modulated reactants. Analytic techniques have been developed to extract the average *c*-axis structure of the unit cell, the distribution of *c*-axis crystal sizes, and the distribution of structural defects from X-ray diffraction data. High-resolution synchrotron source X-ray diffraction data were collected from a $[(Fe_{0.33}NbSe_2)_8(Fe_{0.33}TiSe_2)_8]_{12}$ sample (i.e., 12 superlattice unit cells in the film, each cell containing 8 layers of $Fe_{0.33}NbSe_2$ followed by 8 layers of $Fe_{0.33}TiSe_2$) at three anomalously scattering wavelengths. Analysis determined structural parameters within 2% of published values for the parent compounds, typical crystal sizes of 200−500 Å, and typical coherence losses over a unit cell of ±1%. Theoretical diffraction profiles calculated directly from the model structure are shown to agree satisfactorily with experiment. The flexibility offered by our growth technique suggests that synthesis of many such superlattices with a variety of different materials properties should be possible.

Introduction

Among the many important recent trends in materials physics and chemistry, the focus upon exotic materials in which electron correlation plays a significant role and the production of low-dimensional materials and superlattices certainly are two of the most dominant[1,2] A spectacular series of advances has been accomplished in these areas, ranging from the discovery of high-temperature superconductors to giant and colossal magnetoresistance. It is important and useful to continue to develop new materials or new growth techniques that enable rational modification of existing materials systems with an eye toward optimizing useful properties. In this paper, we report application of a new thin film growth technique to produce superlattices of exotic, quasi-2D intercalated transition metal dichalcogenide (TMDC) materials.

Various unusual properties of layered TMDC materials have fueled their study for the last 25 years.[3,4] They exhibit charge density wave effects and additionally form many intercalation complexes which also have unique and interesting properties. Planar, hexagonally coordinated atomic sheets are the structural building blocks of TMDCs. A sheet of parent transition metal atoms is sandwiched between two chalcogen sheets, and such covalently bonded trilayers are stacked one atop the other. Each trilayer is only loosely bound by dispersion forces to its neighbors, leaving a vacant van der Waals gap of approximately 3 Å. The TMDC structure offers many opportunities for rational and systematic variation: (i) many different parent TMDCs and alloys are known, (ii) a wide range of intercalate atoms and molecules can be added in variable mole fraction to the van der Waals gap, (iii) a variety of stackings of hexagonal sheets is possible so polytypes abound, and (iv) a variety of superlattices can be formed if appropriate growth techniques can be developed.

While the host TMDC compounds can be classified as exotic due to the electronic instabilities they exhibit, electron correlation plays a relatively minor role in determining their electronic properties. By contrast, the 3d intercalates of TMDC compounds exhibit a variety of exotic magnetic behaviors supported by the formation of on-site electron-correlation-induced local moments on the intercalant atoms.[5−8] Our focus on the 3d intercalates and superlattices stems from the current interest in magnetoresistance. The observation of giant magnetoresistance (GMR) in metal superlattices[9,10] and the development of room-temperature colossal magnetoresistance (CMR)[11] compounds such as the mixed valence layered manganese perovskites[12] have served to accentuate the potential for such systems in magnetic recording and reading.[13] The CMR compounds have ordered

* Address correspondence to this author.
[†] Department of Physics, University of Oregon.
[‡] Brookhaven National Laboratory.
[§] Department of Chemistry, University of Oregon.

(1) Fuggle, J. C.; Sawatzky, G. A.; Allen, J. W. *NATO ASI Series*; Plenum: New York, 1988; Vol. B184.
(2) Mott, N. F. *Metal−Insulator Transitions*; Taylor & Francis: London, 1990.
(3) Levy, F., Ed. *Crystallography and Crystal Chemistry of Materials With Layered Structures*; D. Reidel Publishing Company: Dordrecht, The Netherlands, 1976.
(4) Wilson, J. A.; DiSalvo, F. J.; Mahajan, S. *Adv. Phys.* **1975**, *24*, 117−201.
(5) Friend, R. H.; Yoffe, A. D. *Adv. Phys.* **1987**, *36*, 1−94.
(6) Inoue, M.; Hughes, H. P.; Yoffe, A. D. *Adv. Phys.* **1989**, *38*, 565−604.
(7) Parkin, S. S. P.; Friend, R. H. *Philos. Mag.* **1980**, *41B*, 65−93.
(8) Parkin, S. S. P.; Friend, R. H. *Philos. Mag.* **1980**, *41B*, 95−112.
(9) Baibich, M. N.; Broto, J. M.; Fert, A.; Van Dau, F. N.; Petroff, F.; Etienne, P.; Creuzet, G.; Friedrich, A.; Chazelas, J *Phys. Rev. Lett.* **1988**, *61*, 2472−2475.
(10) Parkin, S. S. P. *Annu. Rev. Mater. Sci.* **1995**, *25*, 357−388.
(11) Jin, S.; Tiefel, T. H.; McCormack, M.; Fastnacht, R. A.; Ramesh, R.; Chen, L. H. *Science* **1994**, *264*, 413−415.
(12) Moritomo, Y.; Asamitsu, A.; Kuwahara, H.; Tokura, Y. *Nature* **1997**, *380*, 141−144.
(13) Liu, J.; Chang, I. C.; Irons, S.; Klavins, P.; Shelton, R. N.; Song, K.; Wasserman, S. R. *Appl. Phys. Lett.* **1995**, *66*, 3218−3220.

10.1021/ja994140o CCC: $19.00
Published on Web 09/02/2000

magnetic moments, and enhanced scattering near the magnetic ordering temperatures is generally implicated in producing the large magnetoresistance. A similar statement can apparently be made for the bulk 3d intercalation compounds, as evidenced by large anomalies in resistivity and Hall coefficient observed near the Néel or Curie temperature.[5−8] Superlattices composed of 3d TMDC intercalates offer the possibility of combining these two types of anomalous magnetoresistance, intrinsic (CMR) and structure induced (GMR), in one material.[14]

Experimental Section

Making superlattices composed of 3d TMDC intercalates is a formidable synthetic challenge. Molecular beam epitaxy, the standard synthetic route to ordered crystalline superlattices, would be very difficult to apply to these quaternary superlattices.[15,16] Finding suitable growth conditions (deposition rates, substrate temperature, etc.) would be the major challenge as this becomes increasingly difficult as the number of elements involved increases. In addition, new growth conditions would need to be determined for each different intercalant. Therefore, we decided to explore the use of elementally modulated reactants to prepare these compounds. This approach, which takes advantage of the slow diffusion rates of atoms in the solid state, has been shown to be a robust synthetic technique to prepare derivatives of a desired structure.[17] The elementally modulated reactants are made by sequentially depositing, in high vacuum, thin layers (5−20 Å) of reactants, and then annealing this film at increasingly higher temperature until a crystalline superlattice is obtained. The film is deposited with a modulation in composition determined by the modulation in stoichiometry of the desired superlattice. By controlling and systematically varying the subsequent annealing process, we achieve a degree of kinetic control over nucleation and growth while also minimizing interfacial mixing. The details of synthesis of some $NbSe_2$/$TiSe_2$ superlattices have been previously reported in which relatively thick elemental layers (15−16 Å selenium layers) can be used in the modulated reactants.[18,19]

This paper reports synthesis and characterization of $[(Fe_{0.33}NbSe_2)_8(Fe_{0.33}TiSe_2)_8]_{12}$ and $[(Cr_{0.33}NbSe_2)_6/(Cr_{0.33}TiSe_2)_6]_{10}$ superlattices. The reactants were sequentially deposited in a vacuum chamber under a 1×10^{-7} Torr background pressure onto an unheated Si substrate that had been polished smooth to ±3 Å. Three electron gun evaporators provided beams of Nb, Ti, and Fe or Cr, while a Knudsen cell supplied Se, all evaporation rates being precisely controlled by an Inficon crystal monitor. Each beam could be blocked by a computer-controlled shutter. The deposition sequence for the Fe (or Cr) superlattice was Fe (or Cr), Nb, Se repeated eight (or six) times, then Fe (or Cr), Ti, Se repeated eight (or six) times, with the entire cycle repeated twelve (or ten) times. Electron probe microscopy and low-angle X-ray diffraction were used to verify that the sample as deposited had approximately the same net stoichiometry and repeat unit size as the target crystalline superlattice.

The evolution of the structure of the reactants during the crystallization progress was monitored by recording an X-ray diffraction scan, with scattering vector normal to the film surface, after each annealing step. The films were annealed in a nitrogen drybox at 200, 300, 400, and 480 °C for 10 h at each temperature. A sample of these data is shown in Figure 1, where the intensity axis has been magnified by 2 and 5 times for the two lowest temperature anneals as indicated. The diffraction scan of the as-deposited sample contains weak diffraction intensity at the expected angles for the designed superlattice. This implies that samples as deposited contain crystalline domains with

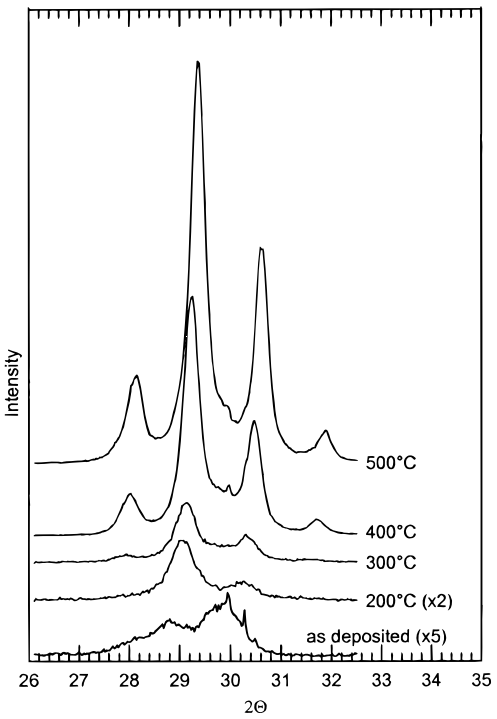

Figure 1. The evolution of the diffraction pattern during annealing. Each scan is offset along the intensity axis by an arbitrary constant. The ×2 and ×5 symbols indicate magnification of the intensity axis.

significant long-range order. As the film is annealed its crystallinity improves and the 00λ diffraction peaks sharpen and shift to higher 2θ values. The persistence of the multiplet structure indicates preservation of the desired crystalline superlattice. Annealing at temperatures above 500 °C broadens the peaks and reduces their intensities. Since the constituent phases of the superlattice are stable at temperatures up to 800 °C, this degradation in the diffraction pattern presumably results from intermixing of phases at the interfaces. Annealed films have been stored in a drybox for over one year and show no degradation in their diffraction pattern. Annealed films in air begin to show diffraction pattern deterioration after a week and are markedly degraded after 5 weeks, presumably due to slow reaction with moisture or oxygen in the air.

The structures of the crystallized films were analyzed using X-ray diffraction. With the scattering vector normal to the film surface, only 00*l* diffraction peaks were observed, indicating that the crystallites orient themselves with this as a common *c*-axis direction. The full width at half of the maximum intensity of the rocking curves of the 00*l* diffraction peaks decrease from approximately 6° in the as-deposited samples to less than 2° for fully annealed samples. This increase in alignment on annealing may be the consequence of easier crystal growth for those crystals with their *c*-axis perpendicular to the substrate. Ostwald ripening during the annealing would then result in the observed narrowing of the rocking curve maxima. A qualitative study of scattering in nonnormal directions indicated no preferred direction in the (*a*,*b*) plane.

To characterize the structure of the films in the *c*-direction high-resolution synchrotron X-ray data were collected from the $[(Fe_{0.33}NbSe_2)_8(Fe_{0.33}TiSe_2)_8]_{12}$ superlattice at beamline X7A at the Brookhaven National Synchrotron Light Source, using a Si(111) channel-cut monochromator and a Ge(220) crystal analyzer, with the sample in symmetric flat-plate reflection geometry. Data were collected at three wavelengths, 0.65394(4), 0.98055(4), and 1.74513(3) Å, i.e., 28, 11, and 7 eV below the K-edges of Nb, Se, and Fe, respectively, to provide additional scattering contrast and allow a better determination of the atom distributions in the *c*-axis layers. Anomalous scattering coefficents calculated with the FPRIME[20] computer code are given in Table 1.

(14) Manoharan, S. S.; Satyalakshmi, K. M.; Prasad, V.; Subramanyam, S. V.; Hegde, M. S. *Curr. Sci.* **1995**, *69*, 356−358.
(15) Koma, A.; Saiki, K.; Sato, Y. *Appl. Surf. Sci.* **1989**, *41/42*, 451−456.
(16) Koma, A.; Yoshimura, K. *Surf. Sci.* **1986**, *174*, 556−560.
(17) Hornbostel, M. D.; Hyer, E. J.; Thiel, J.; Johnson, D. C. *J. Am. Chem. Soc.* **1997**, *119*, 2665−2668.
(18) Noh, M.; Johnson, D. C. *Angew. Chem., Int. Ed. Engl.* **1996**, *35*, 2666−2669.
(19) Noh, M.; Thiel, J.; Johnson, D. C. *Science* **1995**, *270*, 1181−1184.
(20) Cromer, D. T. *J. Appl. Crystallogr.* **1983**, *16*, 437.

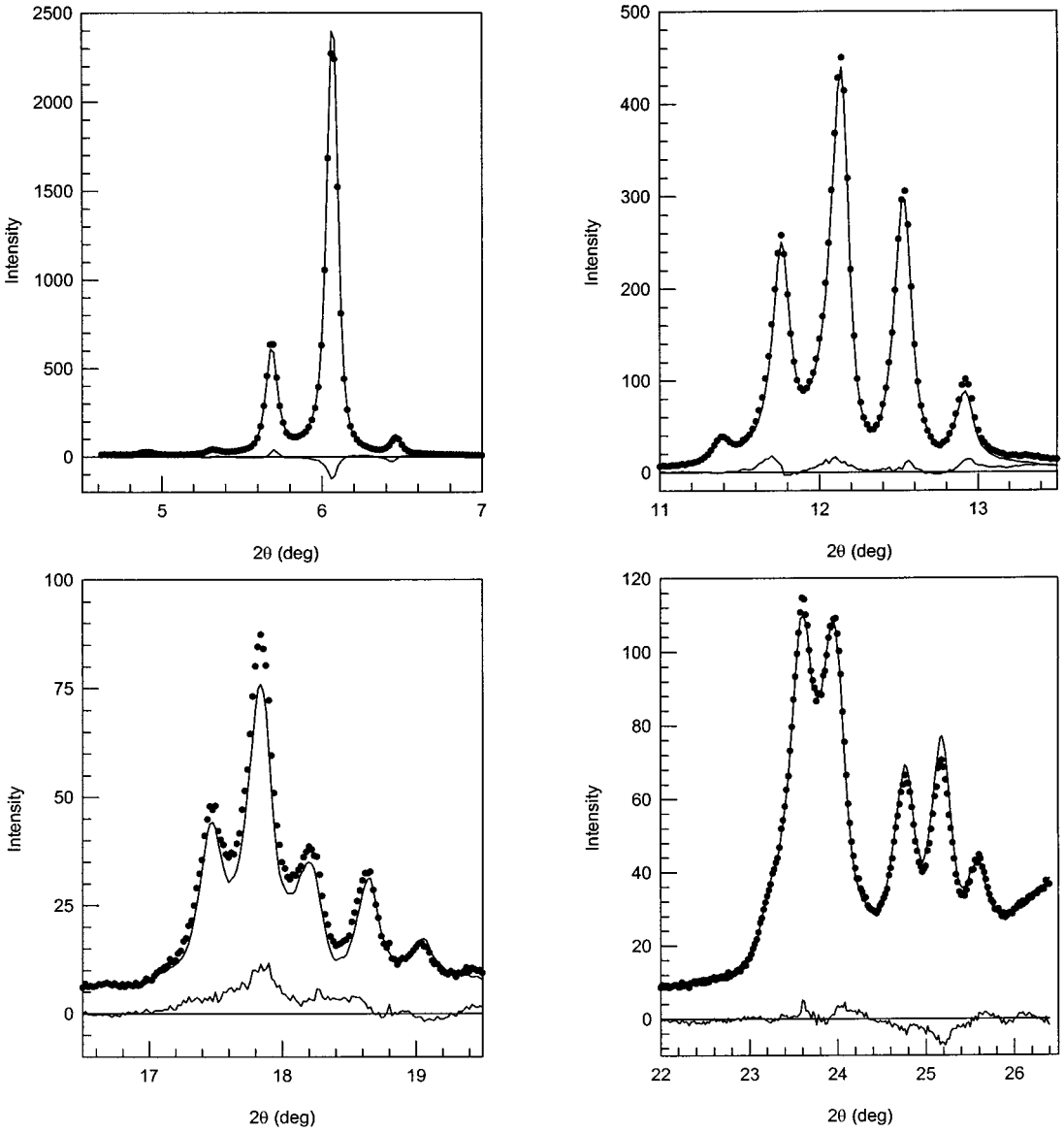

Figure 2. Experimental synchrotron X-ray profiles (dots), calculations (solid line), and residuals (solid line) for the Fe intercalated superlattice at a wavelength of 0.6539 Å.

Table 1. Anomalous Scattering Coefficients f' in Electron Units for Each Element at Each Wavelength

	0.65 Å	0.98 Å	1.75 Å
Nb	−5.99	−0.96	−0.11
Se	−0.01	−6.43	−0.67
Fe	0.29	0.25	−6.70
Ti	0.22	0.33	−0.03

Diffraction data for the $[(Cr_{0.33}NbSe_2)_6/(Cr_{0.33}TiSe_2)_6]_{10}$ superlattice were collected with a Scintag $\theta-\theta$ diffractometer using Cu Kα radiation.

Structural refinement by a fit to observed integrated intensities was unsatisfactory because (i) asymmetric and incommensurate peaks unsuited to standard Rietveld refinement were observed, (ii) significant peak overlap caused large uncertainties in determining integrated intensities, and (iii) some reflections could not be fit by refinement of the unit cell. Thus it appeared the superlattices had insufficient long-range order for application of standard X-ray diffraction analysis techniques, and to characterize the samples, it was necessary to fit the diffraction profile with a model that explicitly included effects of finite crystal size and losses of structural coherence. We set out to quantify the average lattice, the approximate distribution of crystal sizes, and the approximate deviations from the average lattice.

Each sample was modeled with 300 crystals. Scattering from the crystals was summed incoherently to calculate a theoretical diffraction profile. Lattice parameters for an average unit cell, sizes, and defects of the crystals were free parameters of the fit. The defects were incommensurate spacings between trilayers intended to roughly quantify the rate of loss of coherence, and were introduced because finite size alone could not explain the breadth of the diffraction peaks. In summary, the 300 crystals were constructed with a common unit cell, but each with its own size and its own set of defects. Unit cell parameters, represented by unconstrained decimal numbers, were refined using Powell's method.[21] The crystal sizes, constrained to be an integer number of atomic trilayers, and the size and location of the defects (the number of which was fixed, so defects could move, grow, or shrink, but not reproduce) were optimized with a simulated annealing algorithm,[22] a technique suited to discretely variable parameters or situations where good starting values for parameters are not readily available. Additional parameters refined with Powell's method were a scale factor and a temperature factor for each of the three wavelengths where data were collected. The temperature factor, assumed the same for all the atoms, tended to compensate for errors in the powder approximation at low scattering angles.

(21) Will, G. *J. Appl. Crystallogr.* **1979**, *12*, 483−485.
(22) Kirkpatrick, S.; Gelatt, C. D.; Vecchi, M. P. *Science* **1983**, *220*, 671−680.

Simulated annealing proceeds by tentatively changing a structural parameter at random, calculating the change in the goodness of fit, then accepting the modification only if

$$\text{ran} < \exp^{-\Delta E/T} \quad (1)$$

where ΔE is the change in the goodness of fit and ran is a random number between 0 and 1. If the new parameter value improves the fit, ΔE is negative and the change is accepted. If ΔE is positive, the probability of the change being accepted depends on the value of the annealing temperature T. At high T, changes are accepted more liberally. Our measure of goodness of fit was

$$E = \sum (I_{\text{calc}} - I_{\text{obs}})^2/\sigma^2 \quad (2)$$

where I_{calc} and I_{obs} are the calculated and observed intensities at each point on the scan at each wavelength and σ is the uncertainty in I_{obs}. Refinement proceeds from some temperature T by randomly choosing a crystal, randomly varying its size, accepting or rejecting the change according to (1), then, similarly, choosing a defect, moving it or varying its size, and again consulting (1). This is done 500 times, followed by 3 cycles of average structural parameter refinement, then T is reduced by 99% and the process is repeated. When T is so small that very few proposed changes are accepted, the refinement is terminated. We do not address the question of how to optimally generate the random changes or schedule the decrease of T, though such considerations may yield better fits and reduce computer time. The fits which follow required 12 h of CPU time on a 500 MHz DEC Alpha workstation.

We tested our algorithm by fitting scans generated with randomly chosen parameters. Starting from parameter values within 20% of these values, the refinement scheme outlined above returned unit cell parameters to within 0.01% of their initial value, and found crystal size distributions and defect distributions essentially identical to those from the generated scan.

Systematic errors, however, are much larger than uncertainties in the optimization program. The following considerations are relevant. We are primarily interested in long-range atomic order in the sample; that is what X-ray diffraction is most sensitive to. Our model ignores amorphous sample regions, preferential crystal orientation, and temperature diffuse scattering (for example), because they cause only broad, slowly varying features in the scattered X-ray intensity, and so are difficult to quantify compared to longer range effects. Parameters may refine to erroneous values in an attempt to account for features in the diffraction data beyond the scope of our model. To roughly quantify this error, we assume such diffraction features are never sharper than twice the width of the local supperlattice peaks, then consider the family of diffraction scans obtained by adding any such features to the experimental scan for which a fit at least as good as that of Figure 2 can be obtained. That is, a modified experimental scan is calculated, a fit is performed, and if an E value as small as the one from the fit in Figure 2 results, we say we have a plausible state vector. We assume the chance of choosing some modification which strongly couples with the refined parameters is negligibly small. The standard deviation of the set of plausible values for a particular parameter is called the uncertainty for that parameter, and these values are quoted in the Results section. The error bars shown in the following graphs of crystal size distributions and defect distributions are calculated similarly.

Results and Discussion

For the Fe intercalate, Figure 2 shows four regions of the fit to the 0.65 Å scan and the residual. The fits at other wavelengths are comparable. Figure 3 is the refined c-axis projection of the superlattice unit cell; the cell size is 98.95(5) Å. The distances between Fe planes in both regions a and b are within 1% of values published for bulk $Fe_{1/3}NbSe_2$ and $Fe_{1/3}TiSe_2$, and the Nb to Se and Ti to Se distances are within 2% of published values. Crystallographic data for homogeneous samples of the parent compounds show Se, Nb, and Ti atoms displaced alternately above and below the planes indicated in Figure 3

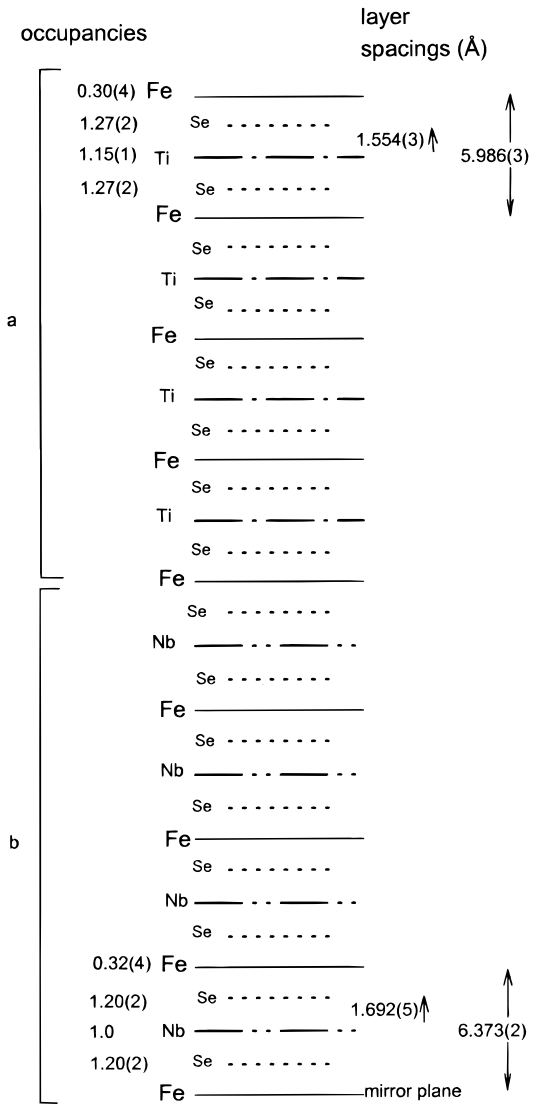

Figure 3. The refined $(Fe_{0.33}NbSe_2)_8(Fe_{0.33}TiSe_2)_8$ superlattice unit cell. For regions "a" and "b", respectively, the distances between Fe planes and between Ti or Nb and Se planes are given. The unit cell size is 98.95(5) Å. The Ti and Nb planes were constrained to lie midway between their neighboring Fe planes. Each pair of Se planes was constrained to sandwich their adjacent Ti or Nb layer symmetrically, and Nb planes were constrained to have an occupancy of 1.0. The occupancy of the central Fe layer was constrained at the average of the adjacent Fe occupancies.

by distances of a few hundredths of an angstrom, but the relatively small effect on the diffraction data of such parameters prevented their refinement. The possible presence of $Fe_{1/4}MX_2$ phases in the sample further obfuscated these parameters.

Figure 4a shows the c-axis size distribution of the crystals. Crystals are most plentiful in the 200−500 Å range, i.e., 2−5 unit cells. Since the physics of superlattices arises from correlation between unit cells, there must be at least 2 unit cells in a crystal to see its effects. Evidently, our sample contains some crystals of the requisite size.

A defect in the sample is modeled as a deviation in the distance between an Fe plane and the Se plane directly below it from the typical distance shown in Figure 3. Introduction of defects into the model was necessary to get even a modest fit to the X-ray diffraction data. In general, it was necessary to include a mechanism for gradual loss of coherence in the model, in addition to the sudden losses of coherence that were introduced via crystals of finite size. The calculated X-ray

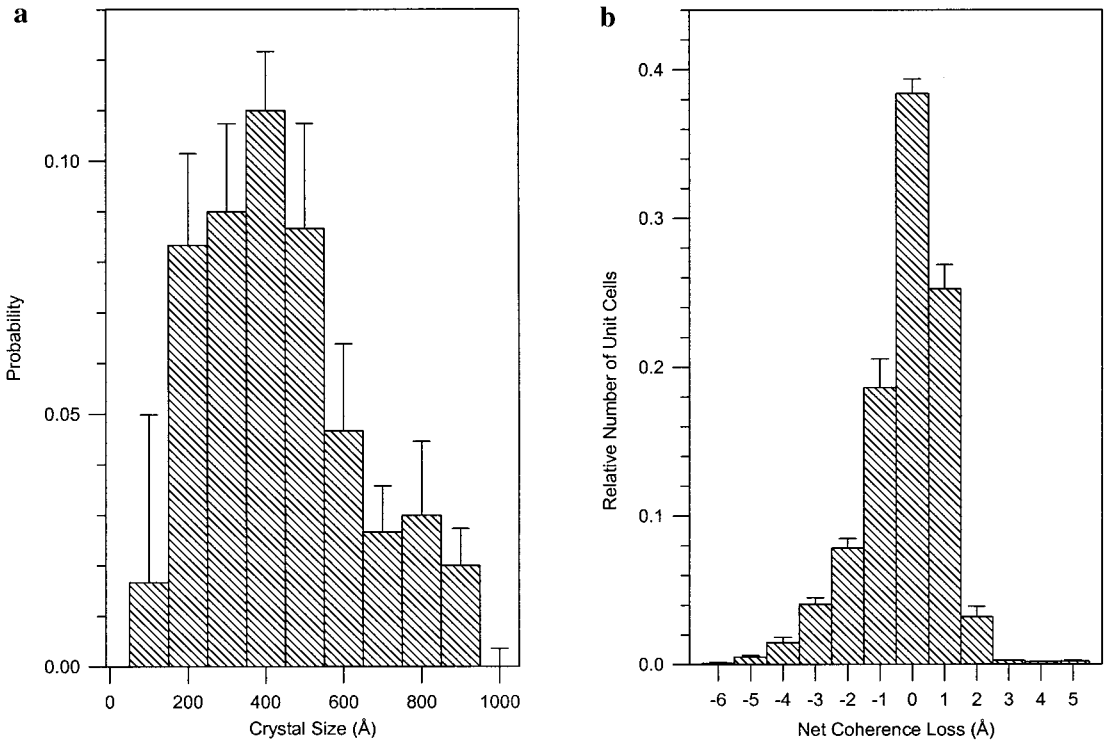

Figure 4. (a) The distribution of crystal sizes. The height of each bar is the probability of a randomly chosen crystal having a size within the range indicated by the width of the bar. (b) The relative number of unit cells with net coherence loss within the horizontal bar dimension.

diffraction pattern is not very sensitive to the details of how long-range coherence is lost. For example, if a model which introduces a single lattice-spacing defect every 150 Å gives a satisfactory fit, so will a model that distributes this defect uniformly among nearby layers. The two calculated scans associated with these two models will not be identical, but their general shapes will be very similar. (This of course is assuming the defects are distributed without correlation). The point is that these two distributions of defects effect equivalent changes in the large length scale registry of the crystal. The calculated diffraction pattern is quite sensitive to changes in the long-range order, so this aspect of the sample should be accurately represented in the refined model.

Consider an Fe plane in the interior of a model crystal. With no defects, an Fe plane that is separated from this one by 15 other Fe planes will be 98.95 Å away—the size of a unit cell. If there are defects, their combined effect may change this distance; the size of this change quantifies the loss of long-range order. Figure 4b shows the probability that the distance between two randomly selected Fe planes (separated by exactly 15 other Fe planes) will deviate from 98.95 Å by various amounts. The salient feature of this presentation is it places less emphasis on two defects of opposite sign the closer they are together, so Figure 4b emphasizes those features of our defect model which are most confidently determined from the diffraction data.

The specific locations of defects in our model, as explained, are not as relevant as their average effects. Nevertheless, some particular aspects of the refined distribution of defects may contain information about the sample. Figure 5 shows the average size for defects appearing at various places in a unit cell. The Fe planes of the cell are numbered 1−16, with 1−7 inclusive being Fe planes with $NbSe_2$ on both sides, 8 with $NbSe_2$ below and $TiSe_2$ above, 9−15 inclusive with $TiSe_2$ planes on both sides, and 16 with $TiSe_2$ below and $NbSe_2$ above. So in Figure 5, the bar above 2, for example, is the average strain

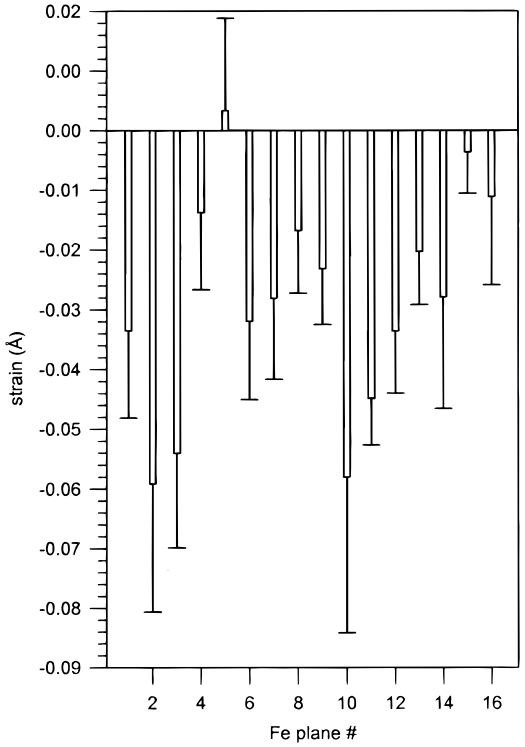

Figure 5. The average size of the defects associated with each Fe plane in the unit cell.

introduced directly below Fe plane 2. Apparently, the net effect of the defects is to reduce the average cell size, but the defects are not strongly correlated with a particular layer of the superlattice unit cell, which is consistent with their being due to off-stoichiometry deposition and impurities rather than lattice mismatch.

Analogous results were obtained for the Cr intercalate, with greater uncertainty in the refined structure since data were

collected at just one wavelength. Refined parameters were again within 2% of published values for bulk materials.

If our superlattices are to display the previously discussed exotic magnetic properties, materials with greater crystallinity must be synthesized. The fitting program we have presented, which gives a direct estimate of crystal sizes and loss of coherence, may be helpful in finding ways to improve the deposition procedure and grow better crystals, to which standard fitting methods may apply. Better control of crystallization, possibly by depositing on a cold substrate so crystal growth only proceeds upon annealing, may be necessary to make samples with larger crystals.

Conclusion

The diffraction results summarized above demonstrate the synthesis of a new class of superlattice containing 3d intercalates of the TMDC parent compounds. The structures obtained show lattice spacings in the *c*-axis direction of the constituent phases agreeing with published values. The growth technique used should be generally applicable to such systems, and synthesis of a diverse array of superlattices with varying magnetic and transport properties should be possible. Growth of additional members of this new family of superlattice materials, as well as the electrical and magnetic characterization of the compounds in hand, is currently underway. Judging from the existing family of magnetic intercalated metal dichalcogenides, we anticipate that the properties of these new compounds may be rich and varied.

Acknowledgment. Work at Brookhaven National Laboratory was supported under Contract No. DE-AC02-98CH10886, U.S. Department of Energy, Division of Materials Sciences. Work at Oregon supported under NSF Grant DMR-9813726.

JA994140O